

# Evidence for multiple nucleosynthetic processes from carbon-enhanced metal-poor stars in the Carina dwarf spheroidal galaxy\*

T. T. Hansen<sup>1</sup>, J. D. Simon<sup>2</sup>, T. S. Li<sup>3</sup>, A. Frebel<sup>4</sup>, I. Thompson<sup>2</sup>, and S. Shectman<sup>2</sup>

- Department of Astronomy, Stockholm University, AlbaNova University Center, 106 91 Stockholm, Sweden e-mail: terese.hansen@astro.su.se
- Observatories of the Carnegie Institution for Science, 813 Santa Barbara St., Pasadena, CA 91101, USA
- <sup>3</sup> Department of Astronomy and Astrophysics, University of Toronto, 50 St. George Street, Toronto ON M5S 3H4, Canada
- Department of Physics & Kavli Institute for Astrophysics and Space Research, Massachusetts Institute of Technology, Cambridge, MA 02139, USA

Received 17 February 2023 / Accepted 26 April 2023

#### **ABSTRACT**

Context. Carbon-enhanced metal-poor (CEMP) stars ([C/Fe] > 0.7) are known to exist in large numbers at low metallicity in the Milky Way halo and are important tracers of early Galactic chemical evolution. However, very few stars of this kind have been identified in the classical dwarf spheroidal (dSph) galaxies, and detailed abundances, including neutron-capture element abundances, have only been reported for 13 stars.

Aims. We aim to derive detailed abundances of six CEMP stars identified in the Carina dSph and compare the abundances to CEMP stars in other dSph galaxies and the Milky Way halo. This is the largest sample of CEMP stars in a dSph galaxy analysed to date. *Methods*. One-dimensional local thermodynamic equilibrium (LTE) elemental abundances are derived via equivalent width and spectral synthesis using high-resolution spectra of the six stars obtained with the MIKE spectrograph at Las Campanas Observatory. *Results*. We derived abundances or upper limits for up to 27 elements from C to Os in the six stars. Our analysis reveals one of the stars to be a CEMP-no star with very low neutron-capture element abundances. In contrast, the other five stars all show enhancements in neutron-capture elements in addition to their carbon enhancement, classifying them as CEMP-s and -r/s stars. The six stars have similar  $\alpha$  and iron-peak element abundances to other stars in Carina, except for the CEMP-no star, which shows enhancement in Na, Mg, and Si. We explored the absolute carbon abundances (A(C)) of CEMP stars in dSph galaxies and find similar behaviour to that seen for Milky Way halo CEMP stars, but highlight that CEMP-r/s stars primarily have very high A(C) values. We also compared the neutron-capture element abundances of the CEMP-r/s stars in our sample to recent i-process yields, which provide a good match to the derived abundances.

**Key words.** stars: abundances – galaxies: dwarf – Galaxy: halo

# 1. Introduction

It has long been recognised that a substantial fraction of the metal-poor stars in the Milky Way (MW) halo show moderate to large enhancements in carbon. These stars, which have [C/Fe] > 0.7, are labelled carbon-enhanced metal-poor (CEMP) stars (Aoki et al. 2007; Beers & Christlieb 2005). Placco et al. (2014) found that 20% of halo stars with [Fe/H] < -2 are CEMP stars, with the fraction increasing with decreasing metallicity. This abundance signature is therefore prevalent in the early Universe, and these stars are important tools for studying early Galactic chemical evolution. The CEMP stars are divided into subcategories depending on their neutron-capture element abundances: CEMP-no stars, which show no enhancement in neutron-capture elements ([Ba/Fe] < 0.0), and the CEMP-r, -s, and -r/s stars, which in addition to carbon also show enhancements in rapid neutron capture (r-)process (CEMP-r: [Eu/Fe] > 1.0), slow

neutron-capture (s-)process elements (CEMP-s: [Ba/Fe] > 1.0, [Ba/Eu] > 0.5), or a combination of both (CEMP-r/s: 0.0 < [Ba/Eu] < 0.5) (Beers & Christlieb 2005).

Radial-velocity monitoring of CEMP-no and CEMP-s stars has revealed that the majority of CEMP-s stars are part of binary systems, while the CEMP-no stars are mostly found to be single stars (Lucatello et al. 2005; Starkenburg et al. 2014; Hansen et al. 2016a,b). These results support the proposed formation scenario for the CEMP-s stars, namely that the peculiar abundance pattern of these stars is the result of mass transfer from a companion that has passed through the asymptotic giant branch (AGB) phase, thus producing C and s-process elements. However, the non-binary nature of the CEMP-no stars suggests they are likely second-generation stars with abundance patterns that are fingerprints of nucleosynthesis processes having taken place in the first generations of stars. Limited radialvelocity monitoring of CEMP-r/s stars suggests that these, like the CEMP-s stars, are also predominantly found in binary systems (Hansen et al. 2016b). The CEMP-no stars therefore provide essential information on the nucleosynthesis of the first stars to form in the Universe, while the CEMP-s and likely r/s stars can be used to gain information about neutron-capture

<sup>\*</sup> Full Tables 6 and B.1 are only available at the CDS via anonymous ftp to cdsarc.cds.unistra.fr (130.79.128.5) or via https://cdsarc.cds.unistra.fr/viz-bin/cat/J/A+A/674/A180

processes in the early Universe as well as mass transfer across binary systems.

Although the abundances of CEMP stars in the MW halo have been the focus of multiple studies (e.g. Aoki et al. 2007; Norris et al. 2013; Hansen et al. 2019), initial spectroscopic exploration of the dSph galaxies has not revealed CEMP stars at similar rates to those found in the halo (Simon et al. 2015; Salvadori et al. 2015). This result is puzzling, as the MW halo is believed to be built via the accretion of surrounding, smaller satellite systems (Searle & Zinn 1978), a conclusion that is strongly supported by the numerous stellar streams discovered in the MW halo in recent large photometric surveys and, in particular, in the data from the Gaia satellite (e.g. Malhan & Ibata 2018; Li et al. 2019). One possible explanation for the apparent rarity of CEMP stars in dwarf galaxies could be the difference in metallicity selection. Many of the halo studies have targeted stars with [Fe/H] < -2.5, whereas relatively few stars in dSphs with [Fe/H] < -2.5 have been studied. Indeed a dedicated search at low metallicity has resulted in 22 CEMP stars being detected in Sculptor, uncovering a CEMP fraction at low metallicity similar to that of the MW halo (Chiti et al. 2018). However, similar dedicated searches for CEMP stars in other dSph galaxies are still lacking.

In addition to the low number of CEMP stars currently discovered in dSph galaxies, even fewer have been subject to high-resolution abundance studies. Therefore, very little is known about the CEMP populations in our dwarf galaxy neighbours, and whether or not they are similar to what we see in the MW halo remains unclear. This paper presents a detailed abundance analysis of six CEMP stars in the Carina dSph galaxy. This is the largest sample of CEMP stars analysed in a dSph galaxy to date. In Sect. 2, we present the observational data for the six stars. The abundance analysis is outlined in Sect. 3, and the results are presented in Sect. 4. Section 5 provides a discussion of our results, and a summary is given in Sect. 6.

# 2. Data

#### 2.1. Observations

The sample stars were first observed as part of a larger search for metal-poor stars in Carina and other dSphs carried out with the IMACS spectrograph (Dressler et al. 2011) on the Magellan/ Baade telescope at Las Campanas Observatory. In the first stage, low-resolution spectra of a total of approximately 1300 candidate Carina stars were obtained with four overlapping slit masks, similar to the process described by Chiti et al. (2018) for Sculptor. Spectroscopic targets were selected from the Carina photometric catalogues available at the Canadian Astronomy Data Centre<sup>1</sup> (Stetson 2000, 2005), which are updated versions of the data originally published by Smecker-Hane et al. (1994). The IMACS spectra were taken through a narrow-band filter targeting the Ca K line to maximise the multiplexing advantage offered by the IMACS field of view. Stars with weak Ca K lines were selected for follow-up observations at medium spectral resolution with the MagE spectrograph (Marshall et al. 2008) on the Magellan/Clay telescope. The MagE spectra cover a wavelength range from 3100 Å to 1 micron and were obtained during four observing runs in 2012 February, 2012 December, 2013 February, and 2013 September using the 0".7 or 1".0 slits (depending on the seeing) and  $1 \times 1$  binning, yielding a resolving power of  $R \sim 4100$ .

Out of a total of 25 Carina stars observed with MagE, 8 exhibited strong C-H features, and we obtained high-resolution spectroscopy for 6 of those with the MIKE spectrograph (Bernstein et al. 2003) at the Magellan/Clay telescope over two runs in 2016 December and 2019 April. The spectra cover a wavelength range of 3350–5000 Å in the blue and 4900–9500 Å in the red and were obtained using a combination of the  $1'' \times 5''$ and  $0.7 \times 5$  slits and  $2 \times 2$  binning, yielding typical resolving powers of 35000 in the blue and 28000 in the red for the  $0.7 \times 5$ " slit and 28 000 in the blue and 22 000 in the red for the 1.0" × 5" slit. The data were reduced with the CarPy MIKE pipeline (Kelson 2003). Table 1 lists our targets (IDs from Fabrizio et al. 2016), total exposure times, and signalto-noise ratios (S/Ns) of the reduced and co-added spectra. In addition, Fig. 1 shows a colour-magnitude diagram of Carina stars using photometry from Fabrizio et al. (2016) with pink star symbols marking the six stars analysed in this work. All photometry has been corrected for reddening using the dust maps from Schlafly & Finkbeiner (2011). Overplotted in red is a Dartmouth isochrone (Dotter et al. 2008) with [Fe/H] = -1.75, age = 12 Gyr, and  $[\alpha/\text{Fe}] = 0.4$ , shifted to the distance of Carina using the distance moduli  $(m-M)_V = 20.05$  mag and  $(m-M)_I =$ 19.98 mag from Mighell (1997), describing the intermediate red giant branch population identified in Fabrizio et al. (2016).

#### 2.2. Radial velocities

The heliocentric radial velocities of our target stars were determined via cross-correlation of the spectra. The MIKE spectra were cross-correlated against the standard star HD 122563 ( $rv_{\text{hel}} = -26.17$  Gaia Collaboration 2018) employing 20 to 50 orders in each spectrum depending on the S/N.

We also measured velocities from the MagE spectra from cross-correlation with the spectrum of 75044 – which has the highest S/N – using between three and eight orders. The heliocentric radial velocity for 75044 was determined to be  $225.7 \pm 1.9 \, \mathrm{km \, s^{-1}}$  using the IRAF task rvidlines, identifying lines of Na (5889, 5895), Mg (5183), and Ba (4934, 5853, 6141). Our final radial velocities are listed in Table 2, along with values from the literature. For the MIKE spectra, we list the standard deviation of radial velocities from the individual orders as the error, while for the MagE spectra, we list the  $1.9 \, \mathrm{km \, s^{-1}}$  velocity error on our template star and the standard deviation of radial velocities from the individual orders added in quadrature.

Inspection of Table 2 reveals that two of the stars, 130624 and 125696, exhibit clear radial-velocity variations consistent with being part of binary systems. We used a  $\chi^2$  test of the probability p that each star's velocity sequence from Table 2 is consistent with a constant velocity to show that  $p \ll 0.05$  for both stars. For 86357 and 40475, the measurements also suggest binary motion, but the uncertainties on some of the measurements are too large to reach firm conclusions. The  $\chi^2$  probabilities for these stars are p=0.27 and p=0.07, respectively, and so further velocity measurements are needed. Finally, our measurements for 97508 (p=0.51) and 75044 (p=0.95) agree with literature values, suggesting no binary motion. However, for 75044, Susmitha et al. (2017) measured radial velocities differing by  $30\,\mathrm{km\,s^{-1}}$  for two epochs for this star². This star is therefore also likely part of a binary.

https://www.canfar.net/storage/list/STETSON/ homogeneous/Carina/

<sup>&</sup>lt;sup>2</sup> Exact radial velocities are not listed in Susmitha et al. (2017).

Table 1. Observation log for MIKE data.

Stellar ID	RA	Dec	Total exp. time	SN at 4500 Å	SN at 6500 Å
75044	06 41 08.58	-50 47 50.1	3 h	20	50
86357	06 41 23.27	-51 13 58.7	4 h 20 min	10	25
130624	06 42 33.03	-505330.7	3 h 20 min	15	25
125696	06 42 23.94	-505403.2	2 h 10 min	12	22
40475	06 40 10.95	-51 01 32.6	5 h 15 min	15	30
97508	06 41 39.95	-504241.3	1 h	7	12

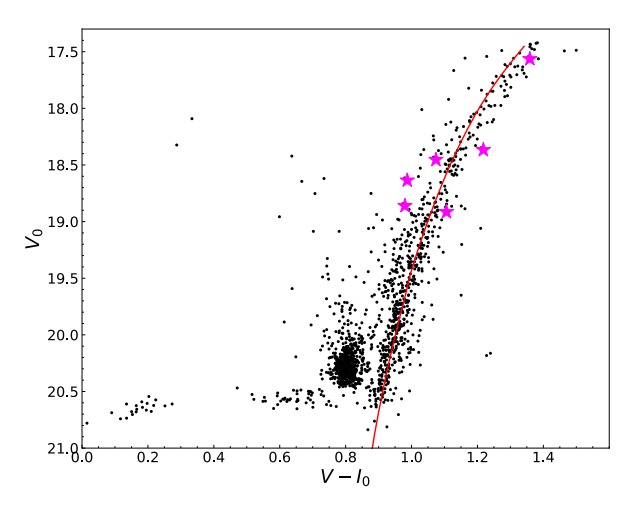


**Fig. 1.** Colour–magnitude diagram for Carina. Black dots are stars identified in Fabrizio et al. (2016), and pink stars are the six stars analysed in this paper. Red curve shows a Dartmouth isochrone (Dotter et al. 2008) with [Fe/H] = -1.75, age = 12 Gyr, and  $[\alpha/Fe] = 0.4$ , shifted to the distance of Carina using the distance moduli  $(m - M)_V = 20.05$  mag and  $(m - M)_I = 19.98$  mag from Mighell (1997).

# 3. Stellar parameter determination and abundance analysis

We determined the effective temperatures  $(T_{\text{eff}})$  of the stars of our sample from V-I, V-J, V-H, V-K, and J-K colours using the empirical relations from Casagrande et al. (2010). V and Imagnitudes are from Fabrizio et al. (2016), and 2MASS JHK magnitudes were taken from Cutri et al. (2003). We corrected all magnitudes for reddening using Schlafly & Finkbeiner (2011). The available photometry varies for the six stars. For 75044, 86357, and 130624, two or more colours were used, including the V-I index, and the final temperature was computed as an average of the individual temperatures. On the other hand, for 125696, 40475, and 97508, only the V-I index could be used. A summary of the photometry and temperature determinations for all stars is listed in Table A.1. B magnitudes are also available for the stars (Fabrizio et al. 2016). However, these are known to be affected by the strong CH bands in CEMP stars, and so we disregard the B-V colours when determining the temperatures of our stars. Following the determination of  $T_{\rm eff}$ , surface gravity ( $\log q$ ), metallicity ([Fe/H]), and microturbulence ( $\xi$ ) were determined spectroscopically from equivalent width (EW) measurements of Fe I and Fe II lines. Atomic data and individual abundances for the Fe lines used in the analysis are listed in Table B.1. The final stellar parameters are presented in Table 3. For the one star where we have temperature estimates from multiple colours (see Table A.1), we find a standard deviation of

**Table 2.** Heliocentric radial velocities for the sample stars.

HJD	$V_{\text{helio}}$ (err) [km s <sup>-1</sup> ]	Ref.	HJD	$V_{\text{helio}}$ (err) [km s <sup>-1</sup> ]	Ref.		
7	75044		8	36357			
2454122.587	222.2(5.7)	1		235.6(11.6)	3		
2456280.828	225.7(1.9)	2	2456280.814	225.1(2.1)	2		
2457744.633	225.5(1.1)	2	2457744.700	227.6(1.3)	2		
2458599.518	225.5(1.0)	2	2457751.599	229.5(1.2)	2		
1	30624		125696				
	210.2(1.6)	3		212.3(8.1)	3		
2454123.555	208.2(6.6)	1	2454122.587	214.3(8.1)	1		
2455982.683	211.7(3.8)	2	2456332.566	221.8(2.8)	2		
2457751.698	218.5(0.7)	2	2457751.806	228.0(0.8)	2		
2457752.842	219.8(1.0)	2					
	10475		ò	7508			
• • •	238.4(10.3)	3		231.8(14.2)	3		
	231.9(1.6)	4	2456331.834	229.5(2.2)	2		
2456329.743	233.6(2.0)	2	2457752.803	232.3(1.0)	2		
2457752.656	236.2(0.7)	2					

**References.** (1) Walker et al. (2009); (2) This work; (3) Fabrizio et al. (2016); (4) Muñoz et al. (2006).

Table 3. Stellar parameters of our target stars.

Stellar ID	T <sub>eff</sub> (±150 K)	$\log g$ (±0.3 dex)	[Fe/H]	$(\pm 0.2  \text{km s}^{-1})$
75044	4140	0.56	$-2.63 \pm 0.11$	2.68
86357	4329	0.97	$-2.87 \pm 0.28$	2.76
130624	4622	0.03	$-2.02 \pm 0.21$	2.14
125696	4868	1.37	$-1.74 \pm 0.22$	2.04
40475	4546	1.16	$-2.73 \pm 0.16$	2.38
97508	4866	1.76	$-2.06 \pm 0.21$	2.36

65 K. However, because fewer colours are used to determine the temperature for most of our stars, we estimate uncertainties on our stellar parameters of 150 K on  $T_{\rm eff}$ , 0.3 dex on  $\log g$ , and 0.2 km s<sup>-1</sup> on  $\xi$ . For the metallicity, the standard deviation of the Fe II line abundances is listed in Table 3. The stars 125696, 40475, and 97508 were also analysed by Koch et al. (2006) who find [Fe/H] =  $-2.33 \pm 0.43$ ,  $-2.66 \pm 0.09$ , and  $-2.22 \pm 0.10$ , respectively, which agree with the values derived in this work within uncertainties<sup>3</sup>.

<sup>&</sup>lt;sup>3</sup> We note that no radial velocities are presented in Koch et al. (2006), but the same data are used to determine the velocities presented in Fabrizio et al. (2016), which are included in Table 2.

We derived abundances for the six stars in Carina via EW analysis and spectral synthesis using the analysis code SMHR<sup>4</sup> to run the 2017 version of the 1D radiative transfer code MOOG<sup>5</sup> (Sneden 1973; Sobeck et al. 2011), assuming local thermodynamical equilibrium (LTE).  $\alpha$ -enhanced ( $[\alpha/Fe] = +0.4$ ) ATLAS9 model atmospheres (Castelli et al. 2003) and line lists generated from linemake<sup>6</sup> (Placco et al. 2021) updated with C-H lines from Masseron et al. (2014)<sup>7</sup> were used as input, and solar abundances were taken from Asplund et al. (2009). The synthesis also includes isotopic and hyperfine structure broadening, where applicable, employing the s-process isotope ratios from Sneden et al. (2008). Table B.1 lists the atomic data for the lines used in the analysis, along with the measured EW and abundance of each line. To determine our final abundances and associated uncertainties, we followed the procedure outlined in Ji et al. (2020a), which computes a mean abundance weighted by the S/N of the individual lines analysed, and the uncertainty calculation includes both systematic and statistical uncertainties as well as co-variance terms between stellar parameters.

# 4. Results

We derive abundances for up to 14 light elements from C to Zn and 13 neutron-capture elements for our six Carina stars. Final abundances are listed in Tables 4 and 5, while Table 6 lists the abundance uncertainties due to stellar parameter uncertainties  $(\Delta_X)$  and the systematic uncertainties  $(s_X)$  for each element in each star.  $s_X$  is based on the line-to-line scatter in the abundances and is included to account for systematic uncertainties in, for example, the atomic data or continuum placement. Abundances for selected elements are plotted in Fig. 2 along with abundances reported in the literature for carbon-normal and CEMP stars in Carina and the MW halo. The abundances for Carina stars (green filled circles) are mainly from Norris et al. (2017), which includes a reanalysis of the data from Shetrone et al. (2003), Venn et al. (2012), and Lemasle et al. (2012). We have also included abundances for additional stars analysed by Koch et al. (2008) and Fabrizio et al. (2015). For the Carina CEMP stars, the data are taken from Abia et al. (2008) (cyan circles) and Susmitha et al. (2017) (yellow circles), while the MW halo carbon-normal (small grey circles) and CEMP (small black circles) star abundances are from Roederer et al. (2014). We note that Roederer et al. (2014) used spectroscopically derived effective temperatures leading to slightly lower metallicities being derived for the stars compared to photometric temperatures as used in this work. However, Roederer et al. (2014) provide homogeneous abundances for a large number of elements, including C, N, K, Zn, and Eu, which are interesting for comparison to the stars analysed here.

## 4.1. CNO abundances

Carbon abundances are derived via synthesis of the C–H G-band at 4300 Å and the  $C_2$  swan band at 5160 Å, when present. In 86357, the C–H band is saturated, and only the  $C_2$  band could be used. Generally, the C abundances are in good agreement between the two bands for the stars when both bands are present and not saturated. Synthesis of the  $C_2$  band for three of the

sample stars with varying C abundances is shown in Fig. 3. An oxygen abundance could only be derived for one of the stars (40475: [O/Fe] = 2.12) from the 6300 Å feature. The star 40475 also exhibits large enhancements in other  $\alpha$ -elements, such as Mg and Si, while this is not the case for the other stars in the sample. Therefore, when deriving C abundances for the rest of the stars, a standard oxygen enhancement for metal-poor stars of [O/Fe] = 0.4 was assumed. All of the stars are significantly enhanced in C and, as such, can be labelled CEMP stars. In Tables 4 and 5, we also list the C abundance corrected for stellar evolutionary effects,  $C_{corr}$ , and these values are plotted in Fig. 2. The corrections were made following Placco et al. (2014) and using the C-H abundances for all stars, except for 86357, where the  $C_2$  abundance was used.

We also investigated the <sup>12</sup>C/<sup>13</sup>C ratio of the stars by fitting <sup>13</sup>C and <sup>12</sup>C lines in a region around 4230 Å. We find that using a <sup>12</sup>C/<sup>13</sup>C ratio of 4 gives a good fit to the spectral regions in all of the stars. This ratio is consistent with the equilibrium value for the CNO cycle, suggesting that the material in all of our stars has been well mixed, as is expected for cool red giants. This would equally apply if any of our binary stars were to have experienced mass transfer, as the companion star would also have had a well-mixed outer layer. After determining the C abundances of the stars, N abundances were derived from the C–N band at 4215 Å for five of the stars (excluding 97508, where the S/N was too low). All five stars exhibit an enhancement in N, which is often also found for halo CEMP stars (Hansen et al. 2015).

# 4.2. Light and iron-peak element abundances

We derived abundances for Na, Mg, Ca, Sc, Ti, Cr, Mn, and Ni for most of our stars, while a Co abundance could only be derived for one star (130624) and Zn for two stars (97508 and 86357). Our analysis provides the first abundances for K derived for any of the stars in Carina, which displays a spread similar to that of most other light-element abundances in Carina. We were not able to derive abundances for Al or V in any of our stars, as the lines were too heavily blended.

# 4.3. Neutron-capture element abundances

In addition to the C enrichment, all but one of the stars (40475) also display large enhancements in neutron-capture elements. In Table 7, we list the [Ba/Fe] and [Ba/Eu] ratios and the corresponding CEMP classification of the stars following Beers & Christlieb (2005). According to this classification, we find one CEMP-no star, three CEMP-s stars, and two CEMP-r/s stars. For the CEMP-no star, abundances of Sr, Y, and Ba are derived, while for the CEMP-s and CEMP-r/s stars, we derive abundance for the neutron-capture elements Y, Zr, Ba, La, Ce, Pr, Nd, Sm, Eu, Gd, and Dy; in some stars, we are also able to derive abundances for Sr, Tb, Lu, and Os.

## 5. Discussion

# 5.1. Comparison to abundances of stars in Carina

As shown in Fig. 2, the  $\alpha$  and iron-peak element abundances we derive for our six sample stars are similar to those of the CEMP and other Carina stars from the literature. The one outlier is the CEMP-no star in our sample, 40475, which has high Mg and Si abundances and is discussed below. Abundances for Sr, Ba, and Eu have previously been derived for a number of stars in Carina. We therefore include panels for these elements in Fig. 2. From

<sup>4</sup> https://github.com/andycasey/smhr

https://github.com/alexji/moog17scat

<sup>6</sup> https://github.com/vmplacco/linemake

https://nextcloud.lupm.in2p3.fr/s/r8pXijD39YLzw5T?
path=%2FCH

**Table 4.** Abundance summary for stars 75044, 86357, and 130624.

			7	5044					8	6357					13	30624		
El.	N	$\log \epsilon (X)$	[X/H]	$\sigma_{ m [X/H]}$ [dex]	[X/Fe]	$\sigma_{\mathrm{[X/Fe]}}$ [dex]	N	$\log \epsilon (X)$	[X/H]	$\sigma_{ m [X/H]}$ [dex]	[X/Fe]	$\sigma_{\mathrm{[X/Fe]}}$ [dex]	N	$\log \epsilon (X)$	[X/H]	$\sigma_{ m [X/H]}$ [dex]	[X/Fe]	$\sigma_{ m [X/Fe]}$ [dex]
С–Н	1	+6.89	-1.54	0.43	+1.12	0.42							1	+7.59	-0.84	0.35	+1.12	0.34
$C_2$	1	+7.05	-1.39	0.34	+1.27	0.34	1	+7.46	-0.97	0.49	+2.05	0.37	1	+7.39	-1.04	0.17	+0.92	0.16
Ccorr		+7.31	-1.12	0.43	+1.54	0.42		+7.71	-0.72	0.49	+2.30	0.37	1	+7.80	-0.63	0.35	+1.33	0.34
C-N	1	+7.39	-0.44	0.63	+2.21	0.63	1	+7.85	+0.02	1.30	+3.04	1.06	1	+7.49	-0.34	0.50	+1.62	0.49
Oı																		
Naı	3	+4.53	-1.71	0.16	+0.95	0.18	2	+3.89	-2.36	0.77	+0.66	0.69	2	+4.62	-1.63	0.39	+0.33	0.37
MgI	2	+5.12	-2.49	0.39	+0.17	0.39	2	+5.36	-2.25	0.88	+0.77	0.70	3	+6.18	-1.43	0.19	+0.53	0.19
SiI																		
Κı	1	+2.98	-2.05	0.32	+0.60	0.30	2	+4.18	-0.86	0.72	+2.16	0.74	1	+3.29	-1.74	0.21	+0.22	0.21
Caı	3	+4.23	-2.11	0.28	+0.55	0.27	5	+4.15	-2.20	0.24	+0.82	0.51	8	+4.77	-1.58	0.09	+0.38	0.11
Sc II	3	+0.29	-2.86	0.18	-0.22	0.23	2	+0.63	-2.53	0.36	+0.35	0.38	3	+0.50	-2.65	0.22	-0.63	0.23
Ti I	2	+2.15	-2.80	0.36	-0.15	0.35	2	+1.86	-3.10	0.35	-0.08	0.53	6	+3.00	-1.95	0.14	+0.01	0.15
Ti II	8	+2.44	-2.52	0.13	+0.12	0.15	6	+2.50	-2.45	0.30	+0.42	0.40	10	+2.81	-2.14	0.11	-0.12	0.20
Cr I	5	+2.74	-2.90	0.16	-0.24	0.18							8	+3.65	-1.99	0.16	-0.03	0.16
Mn I	2	+2.36	-3.07	0.29	-0.42	0.28	2	+2.13	-3.30	0.67	-0.28	0.62	3	+2.78	-2.65	0.17	-0.69	0.18
Fe I	23	+4.85	-2.66	0.11	+0.00	0.00	12	+4.48	-3.02	0.47	+0.00	0.00	46	+5.54	-1.96	0.08	+0.00	0.00
Fe II	3	+4.87	-2.63	0.11	+0.00	0.00	3	+4.64	-2.87	0.28	+0.00	0.00	5	+5.48	-2.02	0.21	+0.00	0.00
CoI													5	+4.23	-1.99	0.14	-0.04	0.15
Ni I	3	+3.49	-2.73	0.38	-0.08	0.38							2	+2.69	-2.30	0.69	-0.34	0.68
Zn I							1	+2.41	-2.15	0.18	+0.86	0.46						
Sr II	1	+0.71	-2.16	0.52	+0.48	0.51							2	+1.10	-1.77	0.34	+0.25	0.33
ΥII	10	+0.77	-1.44	0.09	+1.19	0.12	3	+0.06	-2.15	0.38	+0.72	0.39	11	-0.16	-2.37	0.19	-0.35	0.18
Zr II	5	+1.98	-0.60	0.15	+2.03	0.15							4	+0.78	-1.80	0.23	+0.22	0.23
BaII	3	+1.99	-0.19	0.27	+2.45	0.26	3	+1.75	-0.43	0.87	+2.43	0.83	4	+1.05	-1.13	0.35	+0.90	0.26
La II	10	+0.48	-0.62	0.06	+2.01	0.11	14	+0.53	-0.57	0.16	+2.29	0.30	15	-0.20	-1.30	0.08	+0.72	0.20
Сеп	13	+0.92	-0.66	0.09	+1.98	0.13	6	+0.53	-1.05	0.32	+1.82	0.41	15	+0.37	-1.21	0.10	+0.82	0.20
Pr II	5	+0.00	-0.72	0.15	+1.92	0.14	3	+0.18	-0.55	0.40	+2.32	0.44	5	-0.50	-1.22	0.20	+0.80	0.21
Nd II	16	+0.89	-0.53	0.10	+2.11	0.13	13	+0.65	-0.77	0.15	+2.09	0.28	13	+0.27	-1.15	0.16	+0.87	0.18
Sm II	9	+0.14	-0.82	0.10	+1.81	0.14	6	-0.19	-1.15	0.17	+1.72	0.30	10	-0.48	-1.44	0.13	+0.58	0.18
Eu II	2	-0.70	-1.22	0.46	+1.41	0.45	4	-0.16	-0.68	0.18	+2.18	0.30	2	-1.06	-1.58	0.26	+0.45	0.29
Gd II	4	+0.34	-0.73	0.11	+1.90	0.14	3	+0.29	-0.78	0.71	+2.08	0.70	2	+0.05	-1.02	0.29	+1.00	0.32
Tb II																		
Dуп	2	+0.37	-0.73	0.69	+1.90	0.65							1	-0.41	-1.51	0.37	+0.51	0.31
Lu II	1	-0.61	-0.71	0.28	+1.92	0.24	1	-0.01	-0.11	0.42	+2.75	0.35						
Os I	1	+0.06	-1.34	0.33	+1.32	0.33												

this, we see that the Ba abundance of the CEMP-no star 40475 is in good agreement with Ba abundances for other Carina stars at similar metallicity. Therefore, from this sample, the behaviour of dSph galaxy CEMP stars follows that of the MW halo CEMP stars, with  $\alpha$  and iron-peak element abundances of CEMP-s and r/s stars being similar to other metal-poor stars (Norris et al. 2013; Hansen et al. 2015), while some CEMP-no stars also have distinct light-element abundance signatures.

# 5.2. CEMP stars in dSph galaxies

The first carbon or CH stars in dwarf galaxies were detected more than 40 years ago from low-resolution spectra and in prism surveys. For example, Cannon et al. (1981) obtained spectra of two of the brightest members of Carina, finding both to exhibit strong C<sub>2</sub> bands, while Mould et al. (1982) discovered eight carbon stars in Carina (including the two from Cannon et al. 1981) in their prism survey. Later, Azzopardi et al. (1985, 1986) carried out an extensive prism survey for carbon stars in the dwarf spheroidals Sculptor, Carina, Leo I, Leo II, Draco, and Ursa Minor and presented a list of spectroscopically confirmed carbon stars in Azzopardi et al. (1986). High-resolution follow-up for detailed chemical analysis was not possible at the time and is still a challenge due to the faint nature of the stars. However, although the sample presented here constitutes the largest sample of CEMP stars in a dSph for which a detailed abundance analysis has been carried out, a few CEMP stars in other dSph galaxies have also been analysed previously, including stars discovered by Azzopardi et al. (1985). We searched the literature for stars with both C and neutron-capture element abundances reported. After correcting the reported C abundances for evolutionary effects following Placco et al. (2014), we find CEMP-no, s, and r/s stars in the following dSph galaxies: Carina, Draco, Sextans, Sagittarius, Sculptor, and Ursa Minor.

In Draco, the star 19219 analysed by Cohen & Huang (2009) qualifies as a CEMP star after C correction. These authors derive a Ba abundance of [Ba/Fe] = -0.55. Therefore, the star is a CEMP-no star. Cohen & Huang (2009) reported a radial velocity for the star of  $-295.7 \, \mathrm{km \, s^{-1}}$ , which is in very good agreement with the recent value of  $-296.5 \pm 2.3 \, \mathrm{km \, s^{-1}}$  reported by Massari et al. (2020), suggesting that the star is not in a close binary system.

One CEMP star, S15-19, located in Sextans, was analysed by (Honda et al. 2011), who found it to be Ba- but not Euenhanced, resulting in a CEMP-s label. These authors also found evidence of radial velocity variations, suggesting that the star belongs to a binary system. One CEMP star was also identified in Sagittarius by Sbordone et al. (2020). The authors found that star to have roughly equal enhancements of Ba and Eu, labelling it a CEMP-r/s star. Three consistent radial velocities are reported for the star by Sbordone et al. (2020), providing no evidence for binary motion.

In Sculptor, four CEMP stars have been analysed. First, a CEMP-no star, ET0097, was discovered by

**Table 5.** Abundance summary for Stars 125696, 40475, and 97508.

			12	25696					4	0475					9	7508		
El.	N	$\log \epsilon (X)$	[X/H]	$\sigma_{ m [X/H]}$ [dex]	[X/Fe]	$\sigma_{ m [X/Fe]}$ [dex]	N	$\log \epsilon (X)$	[X/H]	$\sigma_{ m [X/H]}$ [dex]	[X/Fe]	$\sigma_{\mathrm{[X/Fe]}}$ [dex]	N	$\log \epsilon (X)$	[X/H]	$\sigma_{ m [X/H]}$ [dex]	[X/Fe]	$\sigma_{ m [X/Fe]}$ [dex]
С–Н	1	+7.91	-0.52	0.38	+1.20	0.35	1	+6.75	-1.68	0.30	+1.11	0.28	1	+7.12	-1.31	0.57	+0.70	0.47
$C_2$	1	+8.20	-0.23	0.19	+1.49	0.18	1	+7.14	-1.29	0.21	+1.50	0.19						
$C_{corr}$		+8.03	-0.40	0.38	+1.32	0.35		+7.17	-1.26	0.30	+1.53	0.28		+7.29	-1.14	0.57	+0.87	0.47
C-N	1	+8.38	+0.55	0.57	+2.27	0.54	1	+6.96	-0.87	0.49	+1.92	0.47						
Oı							4	+8.02	-0.67	0.11	+2.12	0.15						
Naı	2	+4.75	-1.49	0.41	+0.23	0.38	4	+4.56	-1.68	0.18	+1.11	0.18	2	+4.50	-1.74	0.42	+0.27	0.34
MgI	4	+5.80	-1.80	0.18	-0.08	0.20	5	+6.17	-1.43	0.15	+1.36	0.15	3	+5.43	-2.17	0.24	-0.16	0.23
SiI							2	+5.85	-1.66	0.13	+1.13	0.14						
Κı	1	+3.87	-1.16	0.25	+0.56	0.25	1	+2.70	-2.33	0.16	+0.46	0.16						
Caı	12	+5.05	-1.29	0.12	+0.43	0.16	8	+3.82	-2.53	0.14	+0.26	0.14	6	+4.39	-1.95	0.23	+0.06	0.26
Sc II	1	+0.76	-2.39	0.24	-0.64	0.27	4	-0.05	-3.20	0.15	-0.48	0.15	3	+0.70	-2.45	0.34	-0.39	0.36
TiI	5	+3.31	-1.64	0.16	+0.08	0.20	4	+2.42	-2.53	0.27	+0.26	0.25						
Ti II	6	+2.98	-1.97	0.12	-0.23	0.24	7	+2.45	-2.50	0.26	+0.22	0.18	9	+2.76	-2.20	0.25	-0.13	0.20
CrI	6	+4.12	-1.52	0.12	+0.20	0.17	4	+2.72	-2.92	0.22	-0.13	0.20	4	+3.57	-2.07	0.33	-0.06	0.34
MnI	4	+2.99	-2.44	0.18	-0.72	0.20	3	+1.74	-3.69	0.48	-0.91	0.46						
Fe I	30	+5.78	-1.72	0.12	+0.00	0.00	52	+4.71	-2.79	0.09	+0.00	0.00	24	+5.49	-2.01	0.24	+0.00	0.00
Fe II	2	+5.76	-1.74	0.24	+0.00	0.00	5	+4.77	-2.73	0.16	+0.00	0.00	5	+5.44	-2.06	0.21	+0.00	0.00
Coı																		
Ni I							2	+3.19	-3.03	0.26	-0.24	0.25	3	+4.33	-1.89	0.26	+0.11	0.24
ZnI													1	+2.67	-1.89	0.33	+0.11	0.38
Sr II							1	+0.08	-2.79	0.32	-0.06	0.32						
ΥII	6	+0.50	-1.71	0.15	+0.03	0.24	2	-0.74	-2.95	0.27	-0.22	0.23	4	+0.70	-1.51	0.32	+0.55	0.29
Zr II	4	+1.58	-1.00	0.19	+0.75	0.23							3	+0.96	-1.62	0.23	+0.44	0.25
BaII	4	+2.07	-0.11	0.26	+1.63	0.28	4	-1.73	-3.91	0.21	-1.18	0.15	5	+1.64	-0.55	0.36	+1.52	0.26
La II	14	+0.60	-0.50	0.10	+1.24	0.25							8	+0.70	-0.40	0.25	+1.66	0.23
Ce II	8	+0.98	-0.60	0.10	+1.15	0.26							9	+0.78	-0.80	0.15	+1.27	0.20
Pr II	5	+0.36	-0.36	0.17	+1.39	0.28							3	+0.18	-0.54	0.33	+1.52	0.25
NdII	20	+0.85	-0.57	0.13	+1.18	0.24							8	+0.83	-0.59	0.21	+1.47	0.21
SmII	9	+0.45	-0.51	0.13	+1.24	0.25							7	+0.29	-0.67	0.29	+1.39	0.22
Eu II	3	-0.26	-0.78	0.12	+0.96	0.24							2	-0.41	-0.93	0.38	+1.13	0.33
Gd II	1	+0.74	-0.33	0.29	+1.41	0.40												
Tb II	1	-0.43	-0.73	0.22	+1.02	0.26												
Dy II	1	+0.57	-0.54	0.43	+1.21	0.37							1	+0.86	-0.24	0.41	+1.82	0.40
LuII																		
Os I													1	+1.69	+0.29	0.60	+2.30	0.57

Skúladóttir et al. (2015). These authors find that the star has  $\alpha$  and iron-peak abundances resembling those of other Sculptor stars but that it shows an enhancement in the light neutron-capture elements Sr and Y ([Sr/Fe] = 0.71 and [Y/Fe] = 0.34), leading the authors to suggest that it was polluted by a weak r-process. In a later study, the radial-velocity measurements for this star were explored, revealing a variation of >7 km s<sup>-1</sup> over a period of nine years, leading the authors to suggest that it is a binary (Skúladóttir et al. 2017). Salgado et al. (2016) analysed the star Scl-1013644 and found high C and Ba abundances, concluding that it is a CEMP-s star. However, the star was previously analysed by Geisler et al. (2005), who derived a similar Ba abundance to Salgado et al. (2016), but also derived an Eu abundance for the star resulting in [Ba/Eu] = 0.44. Hence, the star is actually a CEMP-r/s star. The other two CEMP stars in Sculptor have high Ba abundances and may be CEMP-s stars (Lardo et al. 2016). However, no Eu abundances have been derived for the stars, and therefore an r/s classification cannot be excluded. Multiple radial-velocity measurements have not been reported in the literature for any of these stars, rendering their binary nature unknown.

Abundances of neutron-capture elements have been derived for three CEMP stars in Ursa Minor. Two stars, UMiJI19 and UMi33533, were analysed by Cohen & Huang (2010), who also found the stars to have low Ba abundances ([Ba/Fe] = -1.16 and -0.99 respectively), resulting in a CEMP-no classification. Consistent radial velocities were reported for both of these stars

by the Cohen & Huang (2010) study (-246.2 and -248.9 km s<sup>-1</sup>, respectively) as well as by Spencer et al. (2018) ( $-245.6 \pm 0.3$  and  $-249.4 \pm 0.3$  km s<sup>-1</sup>) and Pace et al. (2020) ( $-243.0 \pm 2.2$  and  $-250.2 \pm 2.2$  km s<sup>-1</sup>), suggesting that they are not binaries. In Ursa Minor, Kirby et al. (2015) also found the star Bel60017 to be a CEMP star, and Duggan et al. (2018) later derived a Ba abundance of [Ba/Fe] = 1.26 for the star. Therefore, the star is either a CEMP-s or r/s star. Three consistent radial velocity measurements are reported in the literature for this star ( $-250.0 \pm 5.9$  km s<sup>-1</sup>; Armandroff et al. 1995,  $-246.2 \pm 2.1$  km s<sup>-1</sup>; Kirby et al. 2010, and  $-248.4 \pm 0.6$  km s<sup>-1</sup>; Spencer et al. 2018), providing no evidence that the star is a binary.

Finally, abundances from high-resolution spectra have been reported for three CEMP stars in Carina prior to this study. Abia et al. (2008) analysed two carbon-rich stars, ALW-6 and ALW-7, identified by Azzopardi et al. (1986). Abundances for the two stars are plotted as cyan circles in Fig. 2. As can be seen, these stars exhibit very high Ba abundances compatible with the stars being CEMP-s stars. However, no abundance for Eu was derived, and therefore the stars could also be CEMP-r/s stars. Furthermore, the stars were identified as carbon-rich by Azzopardi et al. (1986), and C/O ratios of 5 and 7 were reported for the stars by Abia et al. (2008), but no [C/Fe] ratio has been derived for the stars. More recently, high-resolution spectra of two other stars, ALW-1 and ALW-8, from the Azzopardi et al. (1986) list were obtained by Susmitha et al. (2017), who analysed ALW-8, finding it to be a CEMP-no star. ALW-1 was not

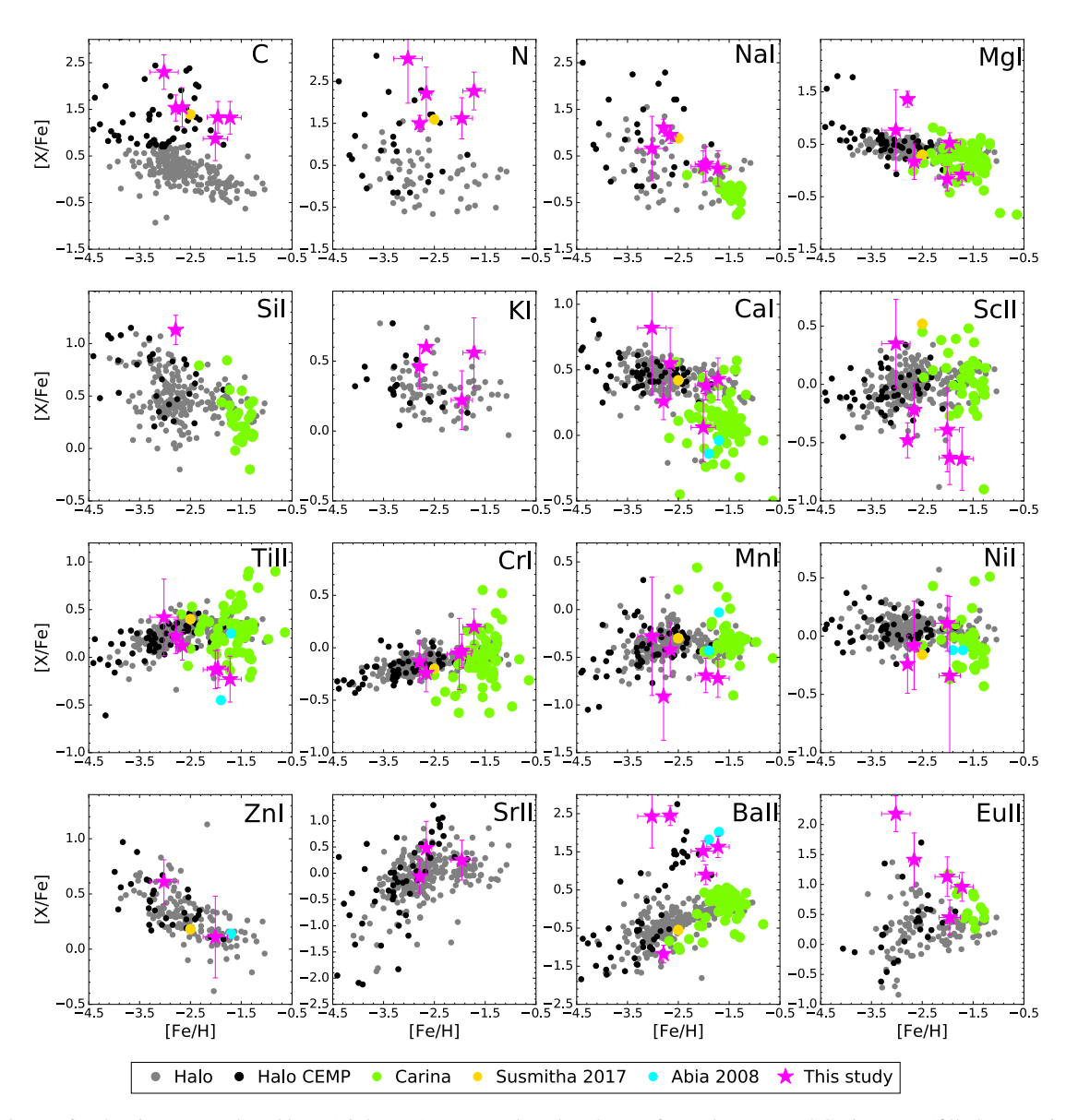


Fig. 2. Abundances for the six stars analysed here (pink stars) compared to abundances for carbon-normal Carina stars (filled green circles), CEMP stars in Carina (yellow and cyan circles), carbon-normal MW halo stars (small grey circles), and CEMP MW halo stars (small black circles). All literature abundances have been converted to the Asplund et al. (2009) solar abundance scale, and all C abundances corrected for evolutionary effects following Placco et al. (2014).

analysed because of its binary nature and low-S/N spectrum. Interestingly, the star rejected by Susmitha et al. (2017) is included in the sample analysed here, namely 75044. The abundances from Susmitha et al. (2017) for the CEMP-no star are plotted as a yellow circle in Fig. 2. These authors find that the star has  $\alpha$  and iron-peak element abundances similar to other Carina stars, and similar to the CEMP-no star in Sculptor, they also find it has a small Y overabundance ([Y/Fe] = 0.29). Finally, Susmitha et al. (2017) do not find evidence of any radial velocity variation for this CEMP-no star.

The results of this literature search combined with the results of the analysis presented here, where we find one CEMP-no, three CEMP-s, and two CEMP-r/s stars in Carina, show us that CEMP stars are indeed present in dSph galaxies. With sufficiently large sample sizes, CEMP stars of the most common types are indeed detected<sup>8</sup>. Also, the CEMP stars in dSphs seem

 $^8$  It should be noted that the rarer, CEMP-r type has not yet been detected in a dSph galaxy.

to have the same binary properties as the halo CEMP stars. However, CEMP stars, and in particular CEMP-no stars, are predominantly found at low metallicities ([Fe/H] < -2), a range that is still not fully explored in many dSph galaxies. Current samples of stars with multiple abundances derived in dSph galaxies primarily contain stars with [Fe/H] > -2.5 (e.g. Norris et al. 2017; Shetrone et al. 2003; Hill et al. 2019). In addition, although C abundances can be derived from medium or low-resolution spectra, high-resolution spectra are required to derive abundances for a number of neutron-capture elements, such as Eu, making it very resource-intensive to gather appropriate samples.

# 5.3. Carbon enhancement as a CEMP classifier

Studies of CEMP stars in the MW halo have revealed a strong relation between CEMP classifications and the level of carbon enhancement the stars exhibit. This was first noticed by Spite et al. (2013), who plotted the absolute C abundance of CEMP

Table 6. Abundance uncertainties.

Stellar ID	El	$\Delta_{T_{\rm eff}}$ [dex]	$\Delta_{\log g}$ [dex]	$\Delta_{\xi}$ [dex]	$\Delta_{[M/H]}$ [dex]	s <sub>X</sub> [dex]
75044	С-Н	0.45	-0.09	-0.09	0.10	0.00
75044	$\mathbf{C}_2$	0.36	0.00	0.00	0.06	0.00
75044	C-N	0.62	-0.04	-0.02	0.22	0.00
75044	Naı	0.15	-0.06	0.00	-0.02	0.08
75044	MgI	0.31	-0.13	-0.07	-0.01	0.42
75044	Κī	0.11	0.04	-0.08	-0.18	0.00
75044	Caı	0.04	-0.00	-0.11	-0.20	0.08
75044	Sc II	-0.13	0.06	-0.06	-0.09	0.10
75044	Ti I	0.37	-0.06	-0.01	-0.05	0.10
75044	Ti II	-0.08	0.05	-0.05	-0.00	0.26
75044	CrI	0.02	-0.03	-0.02	-0.04	0.13
75044	Mn I	0.29	-0.06	-0.03	-0.04	0.10
75044	Fe I	0.07	-0.06	-0.01	-0.02	0.12
75044	Fe II	-0.11	0.11	-0.06	0.05	0.01
75044	Ni I	0.24	-0.02	-0.03	0.00	0.36
75044	SrII	0.03	0.04	-0.14	0.02	0.00
75044	ΥII	-0.06	0.09	0.00	0.01	0.03
75044	Zr II	-0.02	0.05	-0.07	0.02	0.18
75044	Вап	0.17	-0.08	-0.12	0.03	0.16
75044	La II	-0.09	0.10	-0.01	-0.02	0.00
75044	Ce II	-0.07	0.06	-0.03	-0.01	0.15
75044	Pr II	-0.02	0.09	-0.02	0.04	0.16
75044	NdII	-0.06	0.08	-0.02	0.01	0.13
75044	Sm II	-0.08	0.06	-0.04	-0.02	0.18
75044	Eu II	0.08	0.07	-0.02	0.07	0.43
75044	Gd II	-0.09	0.11	0.00	0.00	0.07
75044	Dy II	0.42	0.03	-0.12	0.21	0.36
75044	Lu II	0.21	0.08	-0.00	0.12	0.00
75044	Os I	0.10	0.07	-0.00	-0.09	0.00

**Notes.** The complete version of this table is available at the CDS. Results for one star are shown here to illustrate their form and content.

**Table 7.** Classification of program stars according to Beers & Christlieb (2005).

Stellar ID	[Ba/Fe]	[Ba/Eu]	CEMP type
75044	2.45	1.04	CEMP-s
86357	2.43	0.61	CEMP-s
130624	0.90	0.45	CEMP- $r/s$
125696	1.63	0.67	CEMP-s
40475	-1.18		CEMP-no
97508	1.52	0.39	CEMP- $r/s$

stars as a function of metallicity and discovered two plateaus: A high C plateau at  $A(C) \sim 8.25$  primarily populated by CEMP-s stars and a low C plateau with  $A(C) \sim 6.5$  with mostly CEMP-no stars. This work was extended by Yoon et al. (2016) to include a larger sample and to also account for the change in C abundance as a result of the evolutionary state of the star (Placco et al. 2014), confirming the initial finding.

In Fig. 4, we plot the absolute C abundance (A(C)) as a function of metallicity for our stars, CEMP stars in the halo (Yoon et al. 2016; Goswami et al. 2021; Karinkuzhi et al. 2021; Shejeelammal et al. 2021; Shejeelammal & Goswami 2021, 2022), and dSph CEMP stars from the literature. In addition to the stars listed in the previous section, we also include

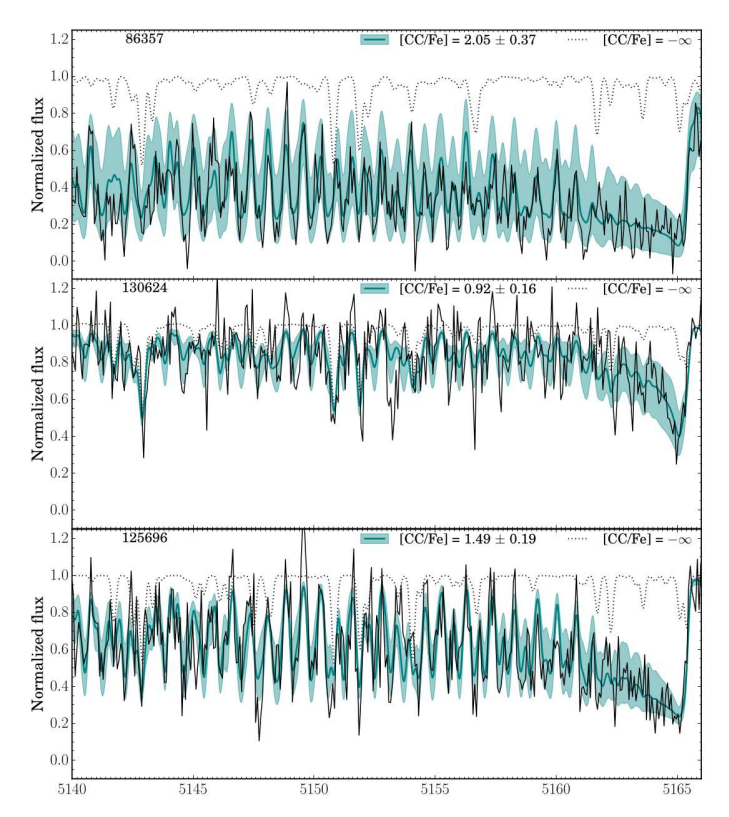


**Fig. 3.** Synthesis of the  $C_2$  band in 86357 (top), 130624 (middle), and 125696 (bottom). Each panel shows the observed spectrum (solid black line) along with a synthesis without C (dotted line), the best-fit synthesis (solid teal line), and uncertainty on the best-fit synthesis (shaded region).

CEMP stars from dSph galaxies for which no neutron-capture element abundances have been derived. In summary, data from the following dSph galaxies are included: Canes Venatici I (Yoon et al. 2020), Carina (Susmitha et al. 2017), Draco (Cohen & Huang 2009; Kirby et al. 2015; Shetrone et al. 2013), Sagittarius (Sbordone et al. 2020), Sculptor (Skúladóttir et al. 2015; Salgado et al. 2016; Geisler et al. 2005; Lardo et al. 2016; Chiti et al. 2018), Sextans (Honda et al. 2011), and Ursa Minor (Kirby et al. 2015; Duggan et al. 2018; Cohen & Huang 2010). All abundances have been converted to the Asplund et al. (2009) solar scale, and C abundances have been corrected for evolutionary effects following Placco et al. (2014). CEMP-no stars are plotted as black symbols, CEMP-s stars in green, CEMPr/s stars in cyan, and CEMP stars with no classification in grey. The high and low A(C) plateau values determined by Yoon et al. (2016) are shown as dashed lines. Looking at Fig. 4, the A(C)abundances of CEMP stars detected in dSph galaxies follow the trend seen in the halo with high A(C) values found in CEMP-s and CEMP-r/s stars at the higher metallicity range, and lower A(C) values found for the more metal-poor CEMP stars. Confirming the unclassified nature of the low A(C) stars found at low metallicity in for example Sculptor as CEMP-no stars would strengthen this picture. However, while A(C) can be used to separate most CEMP-no stars from the bulk CEMP sample, the CEMP-s and r/s stars seem to occupy the same A(C) range, though the CEMP-r/s stars tend to have A(C) > 7.5.

To construct Fig. 4, we used the classification criteria from Beers & Christlieb (2005), which require an Eu abundance to distinguish between CEMP-s and CEMP-r/s stars. However, for a large number of stars, no Eu abundance has been derived. This

is true for 75 of the 131 stars labelled as CEMP-s stars in Yoon et al. (2016), which means the majority of the halo sample, and a couple of the stars from the dSph sample (two stars in Sculptor Lardo et al. 2016 and one in Ursa Minor Kirby et al. 2015; Duggan et al. 2018). We therefore split Fig. 4 into two panels. On the left-hand side, stars with a high Ba abundance but no Eu abundance are included as CEMP-s stars, while these are removed from the right-hand side plot. This exercise shows that the CEMP-r/s stars constitute a significant fraction of the stars with high A(C). In fact, ~40% of the CEMP stars included in the plot with neutron-capture element enhancements are CEMP-r/sstars. Looking at the plot on the right-hand side of Fig. 4 also suggests that the CEMP-r/s stars generally have higher A(C)values than the CEMP-s stars with a broad transition region, which is likely a signature of the surface abundance patterns of their progenitors.

# 5.4. CEMP-no stars with high A(C) values

From Fig. 4, it is evident that the CEMP-no stars, both in the halo and in dSph galaxies, occupy a broad region of the A(C)–[Fe/H] diagram. This led Yoon et al. (2016) to separate the CEMP-no stars into two groups; group II with average low A(C) values and a clear dependence on [Fe/H] and group III with higher A(C)values but no dependence on [Fe/H]. These groups are marked with ellipses in Fig. 4 (adapted from Yoon et al. 2016). Following this grouping of the CEMP-no stars, further radial-velocity studies of CEMP stars found that not only do the CEMP-no and CEMP-s stars have different binary properties, but the two groups of CEMP-no stars also seem to have different binary properties. CEMP-no stars with high A(C) are more likely to be binaries than CEMP-no stars with low A(C) (Arentsen et al. 2019). The two CEMP-no stars in Carina and the one in Sculptor have high A(C) values, while the CEMP-no stars in Ursa Minor and Draco have lower A(C) values (see Fig. 4). The CEMP-no star detected in this work, 40475, is likely a binary, as is the CEMP-no star in Sculptor (Skúladóttir et al. 2017), which is consistent with their high A(C) values. However, radial velocity variations have not been detected for the other Carina CEMP-no star, and the Draco and Ursa Minor CEMP-no stars appear to be single as well (see Sect. 5.2), which is in line with their low A(C) values.

In a recent study, Yoon et al. (2019) explored the location of dSph CEMP-no stars in the A(C)-[Fe/H] diagram and found that the majority of the CEMP-no stars in dSph galaxies fall in group II. As can be seen in Fig. 4, this is consistent with our findings. Yoon et al. (2019) suggest this is due to the extended star formation and chemical evolution of the dSph galaxies resulting in a strong metallicity dependence for CEMP stars formed in these environments. These authors also suggest that this can explain the correlation between A(C), A(Na), and A(Mg) found for group II halo CEMP-no stars (Yoon et al. 2016). Our CEMP-no star exhibits very high Na, Mg, and Si abundances (see Fig. 2). This signature has been seen in several CEMP-no stars found in the MW halo (Yoon et al. 2016, and references therein) and in ultrafaint dwarf galaxies (Boötes I: Lai et al. 2011; Gilmore et al. 2013, Segue 1: Norris et al. 2010, Carina III: Ji et al. 2020b). However, for the MW stars, most of these are group III CEMP-no stars (with low A(C)). The signature has been suggested to be the result of extensive processing and mixing in a massive metal-free spinstar progenitor (Maeder & Meynet 2015). The other dSph CEMP-no stars do not display this signature, although the CEMP-no stars from Ursa Minor and Draco are enhanced in Al (Cohen & Huang 2009, 2010), a signature also seen in some of the most metal-poor halo CEMP-no stars (Norris et al. 2013).

One abundance signature most of the dSph CEMP-no stars do have in common is high [Sr/Ba] ratios. All except one of the dSph CEMP-no stars listed in Sect. 5.2 have [Sr/Ba] > 0.8 (or [Y/Ba] > 0.8, as not all stars have a Sr abundance reported in the literature) (Cohen & Huang 2010; Skúladóttir et al. 2015; Susmitha et al. 2017), with the exception being the CEMP-no star in Draco, which has [Sr/Ba] = -0.87 (Cohen & Huang 2009). This signature has also been discovered in halo CEMPno stars by Hansen et al. (2019), who suggested CEMP-no stars could be identified based on their Sr to Ba ratio ([Sr/Ba] > 0.75. Following the notion of Yoon et al. (2019) that dSph CEMP-no stars mostly fall into group II, we looked at the [Sr/Ba] ratios of the group II CEMP-no stars from Yoon et al. (2016) and identified 18 that have [Sr/Ba] > 0.8. In the future, studies combining kinematic analysis with results from detailed abundances analysis, as done by Zepeda et al. (2023), will provide important information on the possible accretion history of these stars.

# 5.5. Classification of CEMP-r/s stars

According to the Beers & Christlieb (2005) classification, two of our sample stars, 130624 and 97508, qualify as CEMP-r/s stars, meaning they are potentially enhanced in a mixture of r- and s-process elements. The origin(s) of this type of abundance pattern of CEMP stars is still not well understood. First of all, how these stars should be classified remains a matter of debate. The original classification scheme from Beers & Christlieb (2005) is based on the Ba and Eu abundances of the stars (0.0 < [Ba/Eu] < 0.5), but other classification schemes have recently been suggested (see Goswami et al. 2021 for a detailed review).

A classification based on the [Sr/Ba] ratios of the CEMP stars was put forward by Hansen et al. (2019). Unfortunately, due to the absorption lines being saturated or heavily blended, we are only able to derive Sr abundances for three of our stars, 40475, 75044, and 130624. These objects have [Sr/Ba] = +1.12, -1.97, and -0.27, which results in CEMP-no, CEMP-r, and CEMP-s classifications, respectively. Other studies have pointed out that La is a more reliable measure for the s-process contribution in these stars, as more absorption lines of La than of Ba are available in the spectra, and due to the extreme Ba abundances, the Ba lines are often saturated (Karinkuzhi et al. 2021). In addition, the Ba abundances also suffer from non-LTE effects (Korotin et al. 2015). Thus, several studies have suggested using the [La/Eu] ratios of the stars to separate CEMP-s and r/s, where CEMP-r/s stars would have 0.0 < [La/Eu] < 0.5–0.7 (Frebel 2018; Goswami et al. 2021; Karinkuzhi et al. 2021) (the upper limit varies depending on the study). Goswami et al. (2021) also found that most CEMP-r/s stars have [Eu/Fe] > 1, while CEMP-s stars have [Eu/Fe] < 0.

Finally, Karinkuzhi et al. (2021) investigated a classification method based on the distance of the stellar neutron-capture element abundance pattern from the Solar system r-process abundance pattern. Stars enhanced in pure r-process material are known to exhibit a quite robust abundance pattern for the heavy neutron-capture elements, matching that of the scaled Solar System r-process abundance pattern (Sneden et al. 2008). Therefore, in principle, the more r-process dominated a star is, the closer its neutron-capture element abundance pattern will be to the scaled Solar System r-process abundance pattern. Karinkuzhi et al. (2021) calculates a distance to the scaled Solar r-process pattern, d, and finds the CEMP-r/s stars in their sample to have  $0.5 \le d \le 0.8$  while their CEMP-s stars all have d > 0.7. We

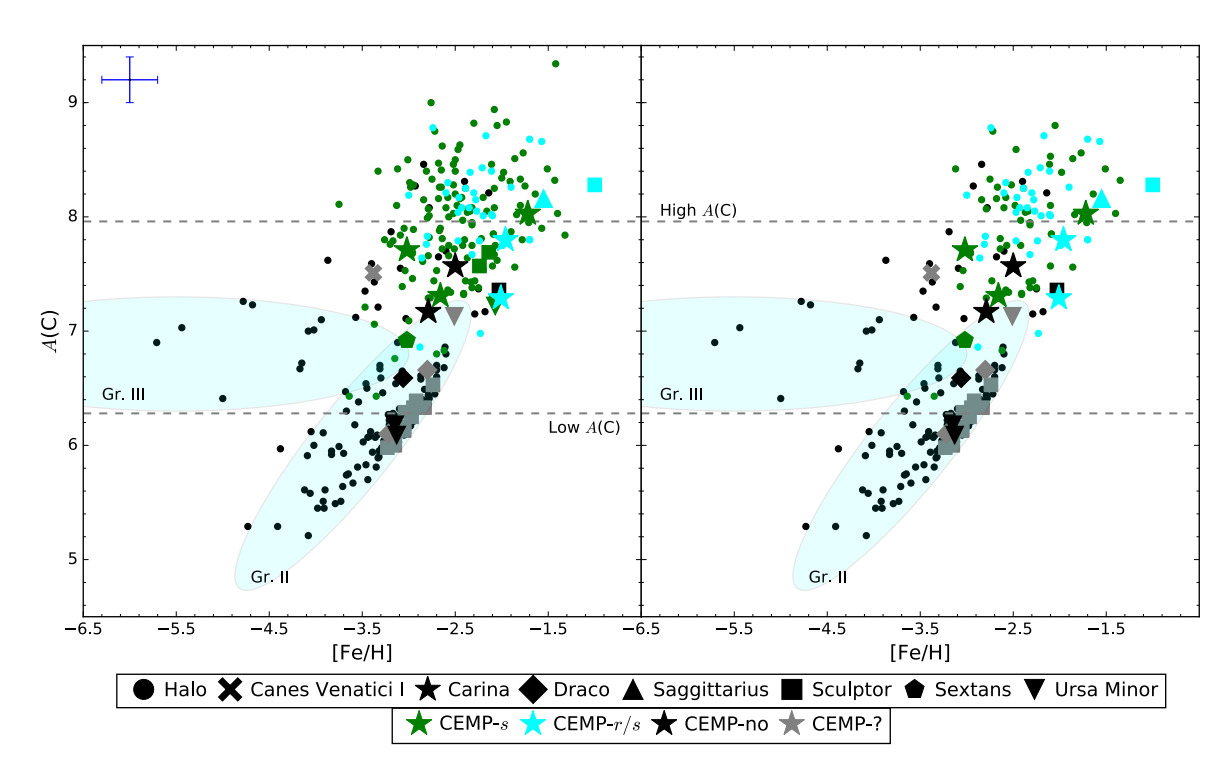


Fig. 4. Absolute carbon abundance as a function of metallicity for CEMP halo stars (filled circles), along with CEMP stars in the galaxies Canes Venatici I (cross), Draco (diamonds), Carina (stars), Sculptor (squares), Sextans (downward pointing triangles), and Ursa Minor (upwards pointing triangles). CEMP-no stars are marked in black, CEMP-s stars in green, CEMP-r/s in cyan, and CEMP stars with no classification are marked in grey. Grey dashed lines indicate the high and low A(C) values as found by Yoon et al. (2016) while the ellipses mark their groups II and III. The left panel shows stars with high Ba abundances but no Eu abundances as CEMP-s stars, while these are removed from the panel on the right.

determined [La/Eu] values and calculated *d* for our stars. The results and re-classifications are listed in Table 8. When calculating *d*, we exclude the light neutron-capture elements Sr, Y, and Zr as the abundances of these elements in *r*-process-enhanced stars have been found to display a larger scatter than abundance for elements heavier than Ba (Hansen et al. 2012; Ji et al. 2016) with respect to Eu, for example. For the stars in our sample, these two methods agree on the classification, and we end up with three CEMP-*r/s* stars in our sample (86357, 130624, and 125696) and two CEMP-*s* stars (75044 and 97508), which is slightly different from the Beers & Christlieb (2005) classification and highlights a likely notable contribution to the abundance patterns of these stars from a nucleosynthesis process with a higher neutron flux than the *s*-process.

The uncertainties on the derived abundances clearly present a limitation to the classification. We estimated this uncertainty by generating 100 sets of 'new' abundances for the stars drawn from a Gaussian distribution in the range  $[X/Fe] \pm \sigma_{[X/Fe]}$  and re-calculating d with these new abundances. The result of this exercise is that d values for the three CEMP-r/s fluctuate in the range from 0.2 to 0.7, while the d values for the two CEMP-s stars lie in the range from 0.2 to 0.9. Therefore, while the d values vary a great deal, the CEMP-r/s stars still stay below (or just at) the d = 0.7 found to be the lower limit for CEMP-s stars in Karinkuzhi et al. (2021).

# 5.6. Origin of CEMP-r/s stars

Many attempts have been made to understand the origin(s) of the peculiar abundance pattern of the CEMP-r/s stars, steadily assuming that both the s- and the r-process indeed contribute to these unusual patterns. Most of the invoked scenarios involve

**Table 8.** Classification of program stars following Karinkuzhi et al. (2021).

Stellar ID	d	[La/Eu]	CEMP type
75044	0.72	0.60	CEMP-s
86357	0.30	0.11	CEMP- $r/s$
130624	0.59	0.27	CEMP-r/s
125696	0.54	0.28	CEMP-r/s
97508	0.73	0.53	CEMP-s

various combinations of r- and s-process events, polluting the star or the gas it formed from; for example, forming a binary system from gas already polluted by an *r*-process event and then invoking mass transfer in the binary system to get the additional C and s-process enrichment (see Jonsell et al. 2006; Abate et al. 2016 for reviews). Sbordone et al. (2020) found that the latter scenario best explained the abundance pattern of the CEMP-r/sstar in the Sagittarius dSph. However, so far, it has only been possible to match a combined r- and s-process pattern to the abundance pattern of one CEMP-r/s star in the MW halo (Gull et al. 2018), which the authors suggest should be relabelled as CEMPr+s to reflect the actual contributions of both of these processes. Therefore, in recent years, the suggestion that a process with a neutron flux intermediate between the r- and s-process, the socalled *i*-process (Cowan & Rose 1977), could create this signature has gained ground (e.g. Hampel et al. 2016).

Currently, various processes in very metal-poor, low-mass AGB stars (Campbell & Lattanzio 2008; Cristallo et al. 2009; Campbell et al. 2010; Stancliffe et al. 2011; Choplin et al. 2021) and super-AGB stars (Doherty et al. 2015; Jones et al. 2016)

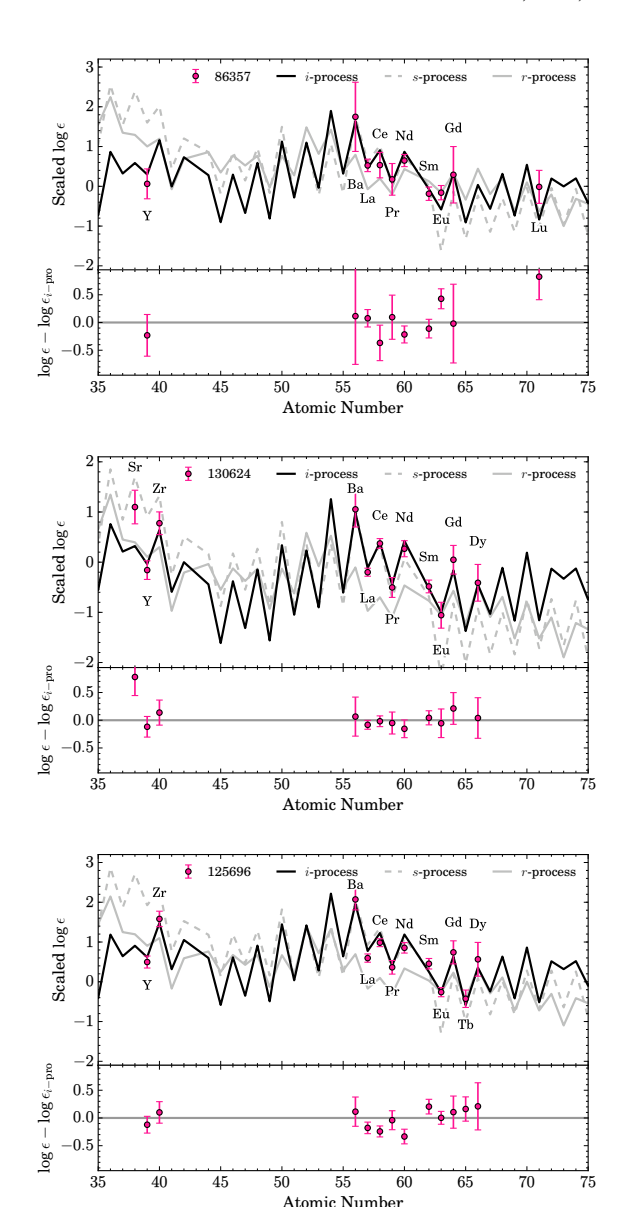


**Fig. 5.** Absolute  $\log \epsilon$  (X) abundances for the three CEMP-r/s stars in our sample compared to scaled i-process yields from Choplin et al. (2022) and the scaled Solar r- and s-process patterns from Sneden et al. (2008). The bottom panel in each plot shows the residual for the match to the i-process yields. The Solar s- and r-process patterns are scaled to the stellar Ba and Eu abundances, respectively, while the average difference between yields and stellar abundances from Ba to Dy was used to scale the i-process yields.

are suggested as *i*-process sources. In addition, conditions required for the *i*-process have also been hypothesised in accreting white dwarfs (Denissenkov et al. 2019) and during the He shell burning phase of metal-free massive stars (Banerjee et al. 2018). Some of these suggested *i*-process sites imply that the CEMP-r/s stars were polluted via mass transfer in a binary system, while others do not. No dedicated radial-velocity monitoring campaign has been published for the CEMP-r/s stars. However, of the three CEMP-r/s stars included in Hansen et al. (2016b), all were found to exhibit radial-velocity variations consistent with belonging to binary systems. For the CEMP-r/s stars detected here, two (125696 and 130624) show clear radial-velocity variations. Therefore, it is likely that the observed signature is a result of binary mass transfer similar to that

of the CEMP-s signature. This is largely in good agreement with i-process conditions being found in specific AGB stars, as mentioned above. In addition, Hampel et al. (2016) compared the abundance patterns of 20 CEMP-r/s stars to i-process model yields from thermally pulsing AGB stars. These authors found that the i-process yields successfully reproduced the neutron/capture abundance pattern of the CEMP-r/s stars, further supporting this scenario. However, this study did not include C abundances as a constraint. In the future, it would be interesting to see if the proposed sites of the i-process can also produce the high C enhancement seen in CEMP-r/s stars.

In Fig. 5, we compare the neutron-capture element abundance patterns of our CEMP-r/s stars to the most recent *i*-process yield available in the literature from Choplin et al. (2022) and the Solar r- and s-process abundance patterns from Sneden et al. (2008). The Solar s- and r-process patterns are scaled to the stellar Ba and Eu abundances, respectively, while the average difference between yields and stellar abundances from Ba to Dy was used to scale the i-process yields. The best fits were obtained using the yields from model M1.0z2.3 with initial mass 1  $M_{\odot}$  and metallicity [Fe/H] = -2.3 for the stars 86357 and 125696, and yields from model M1.0z2.5 with initial mass 1  $M_{\odot}$  and metallicity [Fe/H] = -2.5 for the star 130624. For all three stars, the i-process model yields are generally a good match to the stellar abundances in the element range from Ba to Dy, while some larger discrepancies are seen for the lighter elements Sr, Y, and Zr and for Lu in 86357. In comparison, neither the Solar s- nor r-process patterns display a good match to the stellar abundances. Choplin et al. (2022) also provides yields for C, which for the two models used in Fig. 5 is  $\log_{c}(C) = 9.26$  (M1.0z2.5) and 9.29 (M1.0z2.3). Scaling these using the same scaling as for the neutron-capture elements, we find  $\log_{\epsilon}(C) = 7.24$ , 7.56, and 7.65 for 86357, 12569, and 130624, respectively, which are slightly lower than but almost within uncertainties of the C abundances we derive for the stars  $(\log_{\epsilon}(C_{\text{corr}}) = 7.71 \pm 0.49, 8.03 \pm 0.38, \text{ and } 7.80 \pm 0.35,$ respectively).

# 6. Summary

We present detailed abundances for six CEMP stars in the Carina dSph galaxy. This is the largest sample of CEMP stars in any dSph for which detailed abundances have been derived. Our sample is comprised of one CEMP-no star, three (two) CEMP-s, and two (three) CEMP-r/s stars (depending on the classification criteria).

We find that the CEMP stars have similar  $\alpha$  and iron-peak element abundances to the carbon-normal Carina stars, except for the CEMP-no star, which is highly enhanced in Na, Mg, and Si, a feature also seen in some halo CEMP-no stars. Plotting the absolute C abundance of CEMP stars in dSph galaxies as a function of [Fe/H] reveals a similar trend as that seen for halo CEMP stars with two A(C) groups, where the CEMP-s and r/s stars mostly occupy the higher plateau and the CEMP-no stars the lower plateau. However, we find that the CEMP-r/s stars primarily occupy the highest A(C) range with A(C) > 7.5, though with a notable overlap region between the CEMP-s and r/s stars. The considerable overlap in A(C) values for these two types of CEMP stars highlights the need to derive neutron-capture element abundances in order to identify the CEMP-r/s stars, which will lead to a better understanding of this abundances signature.

Finally, we match the neutron-capture element abundance pattern and C abundances of our CEMP-*r*/*s* stars (Karinkuzhi et al. 2021 classification) to *i*-process yield from metal-poor low-mass AGB models (Choplin et al. 2022), finding a good

match for the elements in the range from Ba to Dy, which strengthens the hypothesis that CEMP-r/s stars show the signature of an intermediate neutron-capture process. However, the models have some trouble reproducing the observed abundances for the light elements and also produce slightly less C compared to the stellar abundances. Therefore, further work is needed to understand the nature of the full abundance pattern of these stars.

Acknowledgements. The authors thank the anonymous referee for their comments, which have improved the manuscript. We thank Josh Adams for his work on the MagE observing program from which the targets of this study were selected. The authors thank Asa Skuladottir for useful discussions on CEMP stars in dwarf galaxies. T.T.H. acknowledges support from the Swedish Research Council (VR 2021-05556). J.D.S. and T.T.H. were partially supported by the NSF through grant AST-1714873. A.F. acknowledges support from NSF CAREER grant AST-1255160 and NSF grant AST-1716251. T.S.L. acknowledges financial support from Natural Sciences and Engineering Research Council of Canada (NSERC) through grant RGPIN-2022-04794. This paper includes data gathered with the 6.5 m Magellan Telescopes located at Las Campanas Observatory, Chile. This research made extensive use of the SIMBAD database operated at CDS, Strasbourg, France (Wenger et al. 2000), arXiv.org, and NASA's Astrophysics Data System for bibliographic information.

# References

```
Abate, C., Stancliffe, R. J., & Liu, Z.-W. 2016, A&A, 587, A50
Abia, C., de Laverny, P., & Wahlin, R. 2008, A&A, 481, 161
Aoki, W., Beers, T. C., Christlieb, N., et al. 2007, ApJ, 655, 492
Arentsen, A., Starkenburg, E., Shetrone, M. D., et al. 2019, A&A, 621, A108
Armandroff, T. E., Olszewski, E. W., & Pryor, C. 1995, AJ, 110, 2131
Asplund, M., Grevesse, N., Sauval, A. J., & Scott, P. 2009, ARA&A, 47, 481
Azzopardi, M., Lequeux, J., & Westerlund, B. E. 1985, A&A, 144, 388
Azzopardi, M., Lequeux, J., & Westerlund, B. E. 1986, A&A, 161, 232
Banerjee, P., Qian, Y.-Z., & Heger, A. 2018, ApJ, 865, 120
Beers, T. C., & Christlieb, N. 2005, ARA&A, 43, 531
Belmonte, M. T., Pickering, J. C., Ruffoni, M. P., et al. 2017, ApJ, 848, 125
Bernstein, R., Shectman, S. A., Gunnels, S. M., Mochnacki, S., & Athey, A. E.
   2003, in Instrument Design and Performance for Optical/Infrared Ground-
   based Telescopes, eds. M. Iye, & A. F. M. Moorwood, SPIE Conf. Ser., 4841,
Biémont, É., Blagoev, K., Engström, L., et al. 2011, MNRAS, 414, 3350
Campbell, S. W., & Lattanzio, J. C. 2008, A&A, 490, 769
Campbell, S. W., Lugaro, M., & Karakas, A. I. 2010, A&A, 522, L6
Cannon, R. D., Niss, B., & Norgaard-Nielsen, H. U. 1981, MNRAS, 196, 1
Casagrande, L., Ramírez, I., Meléndez, J., Bessell, M., & Asplund, M. 2010,
   A&A, 512, A54
Castelli, F., & Kurucz, R. L. 2003, in Modelling of Stellar Atmospheres, eds. N.
   Piskunov, W. W. Weiss, & D. F. Gray, 210, A20
Chiti, A., Simon, J. D., Frebel, A., et al. 2018, ApJ, 856, 142
Choplin, A., Siess, L., & Goriely, S. 2021, A&A, 648, A119
Choplin, A., Siess, L., & Goriely, S. 2022, A&A, 667, A155
Cohen, J. G., & Huang, W. 2009, ApJ, 701, 1053
Cohen, J. G., & Huang, W. 2010, ApJ, 719, 931
Cowan, J. J., & Rose, W. K. 1977, ApJ, 212, 149
Cristallo, S., Straniero, O., Gallino, R., et al. 2009, ApJ, 696, 797
Cutri, R. M., Skrutskie, M. F., van Dyk, S., et al. 2003, VizieR Online Data
   Catalog: II/246
Den Hartog, E. A., Lawler, J. E., Sneden, C., & Cowan, J. J. 2003, ApJS, 148,
Den Hartog, E. A., Lawler, J. E., Sneden, C., & Cowan, J. J. 2006, ApJS, 167,
Den Hartog, E. A., Lawler, J. E., Sobeck, J. S., Sneden, C., & Cowan, J. J. 2011,
   ApJS, 194, 35
Den Hartog, E. A., Ruffoni, M. P., Lawler, J. E., et al. 2014, ApJS, 215, 23
Den Hartog, E. A., Lawler, J. E., Sneden, C., Cowan, J. J., & Brukhovesky, A.
   2019, ApJS, 243, 33
Denissenkov, P. A., Herwig, F., Woodward, P., et al. 2019, MNRAS, 488, 4258
Doherty, C. L., Gil-Pons, P., Siess, L., Lattanzio, J. C., & Lau, H. H. B. 2015,
   MNRAS, 446, 2599
Dotter, A., Chaboyer, B., Jevremović, D., et al. 2008, ApJS, 178, 89
Dressler, A., Bigelow, B., Hare, T., et al. 2011, PASP, 123, 288
Duggan, G. E., Kirby, E. N., Andrievsky, S. M., & Korotin, S. A. 2018, ApJ, 869,
Fabrizio, M., Nonino, M., Bono, G., et al. 2015, A&A, 580, A18
Fabrizio, M., Bono, G., Nonino, M., et al. 2016, ApJ, 830, 126
```

```
Frebel, A. 2018, Annu. Rev. Nucl. Part. Sci., 68, 237
Gaia Collaboration 2018, VizieR Online Data Catalog: I/345
Geisler, D., Smith, V. V., Wallerstein, G., Gonzalez, G., & Charbonnel, C. 2005,
   AJ, 129, 1428
Gilmore, G., Norris, J. E., Monaco, L., et al. 2013, ApJ, 763, 61
Goswami, P. P., Rathour, R. S., & Goswami, A. 2021, A&A, 649, A49
Gull, M., Frebel, A., Cain, M. G., et al. 2018, ApJ, 862, 174
Hampel, M., Stancliffe, R. J., Lugaro, M., & Meyer, B. S. 2016, ApJ, 831, 171
Hansen, C. J., Primas, F., Hartman, H., et al. 2012, A&A, 545, A31
Hansen, T., Hansen, C. J., Christlieb, N., et al. 2015, ApJ, 807, 173
Hansen, T. T., Andersen, J., Nordström, B., et al. 2016a, A&A, 586, A160
Hansen, T. T., Andersen, J., Nordström, B., et al. 2016b, A&A, 588, A3
Hansen, C. J., Hansen, T. T., Koch, A., et al. 2019, A&A, 623, A128
Hill, V., Skúladóttir, Á., Tolstoy, E., et al. 2019, A&A, 626, A15
Honda, S., Aoki, W., Arimoto, N., & Sadakane, K. 2011, PASJ, 63, 523
Ivans, I. I., Simmerer, J., Sneden, C., et al. 2006, ApJ, 645, 613
Ivarsson, S., Litzén, U., & Wahlgren, G. M. 2001, Phys. Scr., 64, 455
Ji, A. P., Frebel, A., Simon, J. D., & Chiti, A. 2016, ApJ, 830, 93
Ji, A. P., Li, T. S., Hansen, T. T., et al. 2020a, AJ, 160, 181
Ji, A. P., Li, T. S., Simon, J. D., et al. 2020b, ApJ, 889, 27
Jones, S., Ritter, C., Herwig, F., et al. 2016, MNRAS, 455, 3848
Jonsell, K., Barklem, P. S., Gustafsson, B., et al. 2006, A&A, 451, 651
Karinkuzhi, D., Van Eck, S., Goriely, S., et al. 2021, A&A, 645, A61
Kelson, D. D. 2003, PASP, 115, 688
Kirby, E. N., Guhathakurta, P., Simon, J. D., et al. 2010, ApJS, 191, 352
Kirby, E. N., Guo, M., Zhang, A. J., et al. 2015, ApJ, 801, 125
Koch, A., Grebel, E. K., Wyse, R. F. G., et al. 2006, AJ, 131, 895
Koch, A., Grebel, E. K., Gilmore, G. F., et al. 2008, AJ, 135, 1580
Korotin, S. A., Andrievsky, S. M., Hansen, C. J., et al. 2015, A&A, 581, A70
Kramida, A., Ralchenko, Y., Nave, G., & Reader, J. 2018, APS Meeting
   Abstracts, 2018, M01.004
Kurucz, R., & Bell, B. 1995, Atomic Line Data (R.L. Kurucz and B. Bell)
   Kurucz CD-ROM No. 23 (Cambridge, Mass.: Smithsonian Astrophysical
   Observatory)
Lai, D. K., Lee, Y. S., Bolte, M., et al. 2011, ApJ, 738, 51
Lardo, C., Battaglia, G., Pancino, E., et al. 2016, A&A, 585, A70
Lawler, J. E., & Dakin, J. T. 1989, J. Opt. Soc. Am. B Opt. Phys., 6, 1457
Lawler, J. E., Bonvallet, G., & Sneden, C. 2001a, ApJ, 556, 452
Lawler, J. E., Wickliffe, M. E., den Hartog, E. A., & Sneden, C. 2001b, ApJ, 563,
   1075
Lawler, J. E., Wickliffe, M. E., Cowley, C. R., & Sneden, C. 2001c, ApJS, 137,
Lawler, J. E., Wyart, J. F., & Blaise, J. 2001d, ApJS, 137, 351
Lawler, J. E., Den Hartog, E. A., Sneden, C., & Cowan, J. J. 2006, ApJS, 162,
Lawler, J. E., Sneden, C., Cowan, J. J., Ivans, I. I., & Den Hartog, E. A. 2009,
   ApJS, 182, 51
Lawler, J. E., Guzman, A., Wood, M. P., Sneden, C., & Cowan, J. J. 2013, ApJS,
Lawler, J. E., Sneden, C., & Cowan, J. J. 2015, ApJS, 220, 13
Lemasle, B., Hill, V., Tolstoy, E., et al. 2012, A&A, 538, A100
Li, R., Chatelain, R., Holt, R. A., et al. 2007, Phys. Scr., 76, 577
Li, T. S., Koposov, S. E., Zucker, D. B., et al. 2019, MNRAS, 490, 3508
Ljung, G., Nilsson, H., Asplund, M., & Johansson, S. 2006, A&A, 456, 1181
Lucatello, S., Tsangarides, S., Beers, T. C., et al. 2005, ApJ, 625, 825
Maeder, A., & Meynet, G. 2015, A&A, 580, A32
Malhan, K., & Ibata, R. A. 2018, MNRAS, 477, 4063
Marshall, J. L., Burles, S., Thompson, I. B., et al. 2008, in Ground-based and
   Airborne Instrumentation for Astronomy II, eds. I. S. McLean, & M. M.
   Casali, SPIE Conf. Ser., 7014, 701454
Massari, D., Helmi, A., Mucciarelli, A., et al. 2020, A&A, 633, A36
Masseron, T., Plez, B., Van Eck, S., et al. 2014, A&A, 571, A47
McWilliam, A. 1998, AJ, 115, 1640
Meléndez, J., & Barbuy, B. 2009, A&A, 497, 611
Mighell, K. J. 1997, AJ, 114, 1458
Mould, J. R., Cannon, R. D., Aaronson, M., & Frogel, J. A. 1982, ApJ, 254, 500
Muñoz, R. R., Majewski, S. R., Zaggia, S., et al. 2006, ApJ, 649, 201
Norris, J. E., Gilmore, G., Wyse, R. F. G., Yong, D., & Frebel, A. 2010, ApJ,
   722, L104
Norris, J. E., Yong, D., Bessell, M. S., et al. 2013, ApJ, 762, 28
Norris, J. E., Yong, D., Venn, K. A., et al. 2017, ApJS, 230, 28
O'Brian, T. R., Wickliffe, M. E., Lawler, J. E., Whaling, W., & Brault, J. W.
   1991, J. Opt. Soc. Am. B Opt. Phys., 8, 1185
Pace, A. B., Kaplinghat, M., Kirby, E., et al. 2020, MNRAS, 495, 3022
Pehlivan Rhodin, A., Hartman, H., Nilsson, H., & Jönsson, P. 2017, A&A, 598,
   A102
Pickering, J. C., Thorne, A. P., & Perez, R. 2001, ApJS, 132, 403
```

Pickering, J. C., Thorne, A. P., & Perez, R. 2002, ApJS, 138, 247

```
Placco, V. M., Frebel, A., Beers, T. C., & Stancliffe, R. J. 2014, ApJ, 797, 21
Placco, V. M., Sneden, C., Roederer, I. U., et al. 2021, Res. Notes Am. Astron.
Quinet, P., Palmeri, P., Biémont, É., et al. 2006, A&A, 448, 1207
Roederer, I. U., Lawler, J. E., Sneden, C., et al. 2008, ApJ, 675, 723
Roederer, I. U., Lawler, J. E., Sobeck, J. S., et al. 2012, ApJS, 203, 27
Roederer, I. U., Preston, G. W., Thompson, I. B., et al. 2014, AJ, 147, 136
Ruffoni, M. P., Den Hartog, E. A., Lawler, J. E., et al. 2014, MNRAS, 441, 3127
Salgado, C., Da Costa, G. S., Yong, D., & Norris, J. E. 2016, MNRAS, 463, 598
Salvadori, S., Skúladóttir, Á., & Tolstoy, E. 2015, MNRAS, 454, 1320
Sbordone, L., Hansen, C. J., Monaco, L., et al. 2020, A&A, 641, A135
Schlafly, E. F., & Finkbeiner, D. P. 2011, ApJ, 737, 103
Searle, L., & Zinn, R. 1978, ApJ, 225, 357
Shejeelammal, J., & Goswami, A. 2021, ApJ, 921, 77
Shejeelammal, J., & Goswami, A. 2022, ApJ, 934, 110
Shejeelammal, J., Goswami, A., & Shi, J. 2021, MNRAS, 502, 1008
Shetrone, M., Venn, K. A., Tolstoy, E., et al. 2003, AJ, 125, 684
Shetrone, M. D., Smith, G. H., Stanford, L. M., Siegel, M. H., & Bond, H. E.
   2013, AJ, 145, 123
Simon, J. D., Jacobson, H. R., Frebel, A., et al. 2015, ApJ, 802, 93
Skúladóttir, Á., Tolstoy, E., Salvadori, S., et al. 2015, A&A, 574, A129
Skúladóttir, Á., Tolstoy, E., Salvadori, S., Hill, V., & Pettini, M. 2017, A&A,
  606, A71
Smecker-Hane, T. A., Stetson, P. B., Hesser, J. E., & Lehnert, M. D. 1994, AJ,
```

Sneden, C. A. 1973, PhD Thesis, University of Texas, Austin, USA

108, 507

```
Sneden, C., Cowan, J. J., & Gallino, R. 2008, ARA&A, 46, 241
Sneden, C., Lawler, J. E., Cowan, J. J., Ivans, I. I., & Den Hartog, E. A. 2009,
   ApJS, 182, 80
Sobeck, J. S., Lawler, J. E., & Sneden, C. 2007, ApJ, 667, 1267
Sobeck, J. S., Kraft, R. P., Sneden, C., et al. 2011, AJ, 141, 175
Spencer, M. E., Mateo, M., Olszewski, E. W., et al. 2018, AJ, 156, 257
Spite, M., Caffau, E., Bonifacio, P., et al. 2013, A&A, 552, A107
Stancliffe, R. J., Dearborn, D. S. P., Lattanzio, J. C., Heap, S. A., & Campbell,
   S. W. 2011, ApJ, 742, 121
Starkenburg, E., Shetrone, M. D., McConnachie, A. W., & Venn, K. A. 2014,
   MNRAS, 441, 1217
Stetson, P. B. 2000, PASP, 112, 925
Stetson, P. B. 2005, PASP, 117, 563
Susmitha, A., Koch, A., & Sivarani, T. 2017, A&A, 606, A112
Venn, K. A., Shetrone, M. D., Irwin, M. J., et al. 2012, ApJ, 751, 102
Walker, M. G., Mateo, M., & Olszewski, E. W. 2009, AJ, 137, 3100
Wenger, M., Ochsenbein, F., Egret, D., et al. 2000, A&AS, 143, 9
Wickliffe, M. E., Lawler, J. E., & Nave, G. 2000, J. Quant. Spectrosc. Radiat.
   Transf., 66, 363
Wood, M. P., Lawler, J. E., Sneden, C., & Cowan, J. J. 2013, ApJS, 208, 27
Wood, M. P., Lawler, J. E., Sneden, C., & Cowan, J. J. 2014, ApJS, 211, 20
Yoon, J., Beers, T. C., Placco, V. M., et al. 2016, ApJ, 833, 20
Yoon, J., Beers, T. C., Tian, D., & Whitten, D. D. 2019, ApJ, 878, 97
Yoon, J., Whitten, D. D., Beers, T. C., et al. 2020, ApJ, 894, 7
Yu, Y., & Derevianko, A. 2018, At. Data Nucl. Data Tables, 119, 263
Zepeda, J., Beers, T. C., Placco, V. M., et al. 2023, ApJ, 947, 23
```

# Appendix A: Photometry

**Table A.1.** Photometry and derived  $T_{\text{eff}}$  for the six sample stars.

Stellar ID	V	I	J	Н	K	$T_{\mathrm{eff}}(V-I)$	$T_{\mathrm{eff}}(V-J)$	$T_{\rm eff}(V-H)$	$T_{\rm eff}(V-K)$	$T_{\rm eff}(J-K)$
75044	17.708	16.284	15.235	14.557	14.295	4139	4140			
86357	18.524	17.235	16.270	15.630	15.510	4332	4347	4238	4308	4419
130624	18.629	17.476	16.551	16.039		4672	4595	4599		
125696	18.814	17.747				4868				
40475	19.054	17.885				4546				
97508	19.013	17.965				4866				

References. V and I magnitudes are from Fabrizio et al. (2016) and 2MASS JHK magnitudes were taken from Cutri et al. (2003).

# Appendix B: Atomic data

**Table B.1.** Atomic data and abundances for individual lines analysed.

Stellar ID	Species	λ (Å)	χ (eV)	$\log gf$	EW (mÅ)	σ <sub>EW</sub> (mÅ)	$\log \epsilon(X)$ (dex)	Ref
75044	11.0	5688.20	2.10	-0.41	53.18	6.77	4.46	1
75044	11.0	5889.95	0.00	+0.11	481.72	10.48	4.66	1
75044	11.0	5895.92	0.00	-0.19	368.27	8.08	4.52	1
75044	12.0	5172.68	2.71	-0.19 $-0.36$	246.40	12.37	4.60	2
75044	12.0	5172.00	2.71	-0.30 $-0.17$	455.35	13.94	5.43	$\overset{2}{2}$
75044	19.0	7698.96	0.00	-0.17 -0.18	synth	synth	2.98	1
75044	20.0	6102.72	1.88	-0.13	synth	synth	4.07	3
75044	20.0	6122.22	1.89	-0.31 $-0.33$	-	•	4.07	3
					synth	synth		3
75044 75044	20.0	6161.29	2.52	-1.35	synth	synth	4.11	
75044	21.1	4324.99	0.60	-0.44	synth	synth	0.23	4
75044	21.1	4374.47	0.62	-0.46	synth	synth	0.33	4
75044	21.1	4400.39	0.61	-0.54	synth	synth	0.29	4
75044	22.0	4840.87	0.90	-0.43	45.81	5.04	2.20	5
75044	22.0	5210.38	0.05	-0.82	synth	synth	1.89	5
75044	22.1	4443.80	1.08	-0.71	synth	synth	2.44	6
75044	22.1	4450.48	1.08	-1.52	synth	synth	2.15	6
75044	22.1	4501.27	1.12	-0.77	synth	synth	2.89	6
75044	22.1	4571.97	1.57	-0.31	synth	synth	2.05	6
75044	22.1	5226.54	1.57	-1.26	synth	synth	2.61	7
75044	22.1	5336.79	1.58	-1.60	synth	synth	2.76	6

Notes. The complete version of this table is available at the CDS. A subset is shown here to illustrate its form and content.

References. (1) Kramida et al. (2018); (2) Pehlivan Rhodin et al. (2017); (3) Yu & Derevianko (2018); (4) Lawler & Dakin (1989), using hfs from Kurucz & Bell (1995); (5) Lawler et al. (2013); (6) Wood et al. (2013); (7) Pickering et al. (2001), with corrections given in Pickering et al. (2002); (8) Sobeck et al. (2007); (9) Den Hartog et al. (2011) for both log(gf) value and hfs; (10) O'Brian et al. (1991); (11) Den Hartog et al. (2014); (12) Belmonte et al. (2017); (13) Ruffoni et al. (2014); (14) Den Hartog et al. (2019); (15) Meléndez & Barbuy (2009); (16) Lawler et al. (2015) for log(gf) values and HFS; (17) Wood et al. (2014); (18) Roederer et al. (2012); (19) Biémont et al. (2011); (20) Ljung et al. (2006); (21) Kramida et al. (2018), using HFS/IS from McWilliam (1998) when available; (22) Lawler et al. (2001a), using HFS from Ivans et al. (2006); (23) Lawler et al. (2009); (24) Li et al. (2007), using HFS from Sneden et al. (2009); (25) (Ivarsson et al. 2001), using HFS/IS from Roederer et al. (2008); (28) Lawler et al. (2001b), using HFS/IS from Ivans et al. (2006); (29) Den Hartog et al. (2006); (30) Lawler et al. (2001c), using HFS from Lawler et al. (2001d); (31) Wickliffe et al. (2000); (32) Lawler et al. (2009) for log gf values and HFS; (33) Quinet et al. (2006).